LARGE-EDDY SIMULATION OF THE FLOW AROUND A SURFACE-MOUNTED CUBE USING A DYNAMIC ONE-EQUATION SUBGRID MODEL

Siniša Krajnović and Lars Davidson
Dept. of Thermo and Fluid Dynamics, Chalmers University of Technology
SE-412 96 Gothenburg, Sweden

ABSTRACT
Dynamic one-equation models enable us to predict the reverse transport of turbulent energy. The present paper provides an explanation of this "backscatter" phenomenon. LES was used to study the k equation with the aim of improving RANS models. This work is part of the project entitled "Large Eddy Simulation for Computing the Flow Around Vehicles" (http://www.tfd.chalmers.se/~lada/projects/sinisa /proright.html) in collaboration between the Department of Thermo and Fluid Dynamics at Chalmers and the CFD group at the Volvo Car Corporation.

THE SGS MODEL
The modelled transport equation for the subgrid kinetic energy, k_{sgs}, reads (Davidson 1997a)

$$\frac{\partial k_{sgs}}{\partial t} + (\bar{u}_j k_{sgs})_{,j} = \left(\left(\langle C \rangle_{xyz} \Delta k_{sgs}^{\frac{1}{2}} + \nu \right) (k_{sgs})_{,j} \right)_{,j} + 2\nu_{sgs} \bar{S}_{ij} \bar{S}_{ij} - C_* \frac{k_{sgs}^{\frac{3}{2}}}{\Delta} \quad (1)$$

Here,

$$C = -\frac{\mathcal{L}_{ij} M_{ij}}{2 M_{ij} M_{ij}}; \; M_{ij} = \widehat{\Delta} \widehat{K^{\frac{1}{2}}} \widehat{\bar{S}}_{ij} - \widehat{\Delta k_{sgs}^{\frac{1}{2}} \bar{S}_{ij}}; \quad (2)$$

$$K = \widehat{k_{sgs}} + \frac{1}{2}\mathcal{L}_{ii}$$

where $\mathcal{L}_{ij}$ denotes the *dynamic* Leonard stresses and $K \equiv \frac{1}{2}T_{ii}$ is the subgrid kinetic energy at test level. The coefficient, C_*, has the form

$$C_*^{n+1} = \left(P_K - \widehat{P}_{k_{sgs}} + \frac{1}{\Delta} \widehat{C_*^n k_{sgs}^{\frac{3}{2}}} \right) \frac{\widehat{\Delta}}{K^{\frac{3}{2}}} \quad (3)$$

with

$$P_{k_{sgs}} = -\tau_{ij}^a \bar{u}_{i,j}; \; \tau_{ij}^a \equiv \mathcal{T}_f(u_i, u_j) = -2C\Delta k_{sgs}^{\frac{1}{2}} \bar{S}_{ij}$$

To ensure numerical stability, a constant value of C in space, ($\langle C \rangle_{xyz}$), is used in the momentum equations, which are computed with the requirement that the production in the whole of the computational domain remains the same, i.e.

$$\langle 2C\Delta k_{sgs}^{\frac{1}{2}} \bar{S}_{ij} \bar{S}_{ij} \rangle_{xyz} = 2\langle C \rangle_{xyz} \langle \Delta k_{sgs}^{\frac{1}{2}} \bar{S}_{ij} \bar{S}_{ij} \rangle_{xyz} \quad (4)$$

All local dynamic information is included through the source terms. This is physically sounder as large local variations in C only appear in the source term and the effect of the large fluctuations in the dynamic coefficients is smoothed out. The coefficients in the one-equation model affect the stresses only indirectly. In the standard dynamic model, the C coefficient is linearly proportional to the stresses.

RESULTS
An implicit, two-step time-advancement method is used, Davidson (1997b). Central differencing and Crank-Nicolson are used for space and time discretization, which produces second-order accuracy in space and time.

CHANNEL FLOW
The flow in a plane channel was computed for $Re_\tau = 1050$. A mesh with $64 \times 64 \times 64$ cells was used, with $x_{max} = 2\pi$, $y_{max} = 2$ and $z_{max} = 0.5\pi$. A fairly small extent in the z direction was used in order to obtain a sufficiently good resolution ($z^+_{max} \simeq 26$). The grid is refined near the walls using geometric stretching with an expansion factor of 1.14, which gives $y^+ = 1.1$ for the near-wall node. The time step was set at $\Delta t = 0.0012$, which corresponds to a maximum convective CFL of approximately 0.4. The mean velocity and RMS fluctuations are compared with the LES data produced by Piomelli (1995) in Fig. 1a,b. As can be seen, the agreement is good for all quantities, apart from the streamwise fluctuation, which is over-predicted by some 20%. The dynamic coefficients are presented in Fig. 1c. The time-averaged value of the homogeneous coefficient is $\langle \langle C \rangle_{xyz} \rangle_t \simeq 0.021$. The production, $P_{k_{sgs}}$, is shown in Fig. 1d. It has been split into one positive part and one negative part according to Piomelli et al. (1991)

$$P^+ = \frac{1}{2}\left(P_{k_{sgs}} + |P_{k_{sgs}}|\right)$$

$$P^- = \frac{1}{2}\left(P_{k_{sgs}} - |P_{k_{sgs}}|\right).$$

It can be seen that part of the production is negative (backscatter), thereby reducing the total production, and thereby also k_{sgs} and ν_{sgs}. It should be remembered that, in the dynamic Germano model, only very small magnitudes of negative ν_{sgs} are permitted, but that the magnitude of negative ν_{sgs} is not limited in any way in the present model.

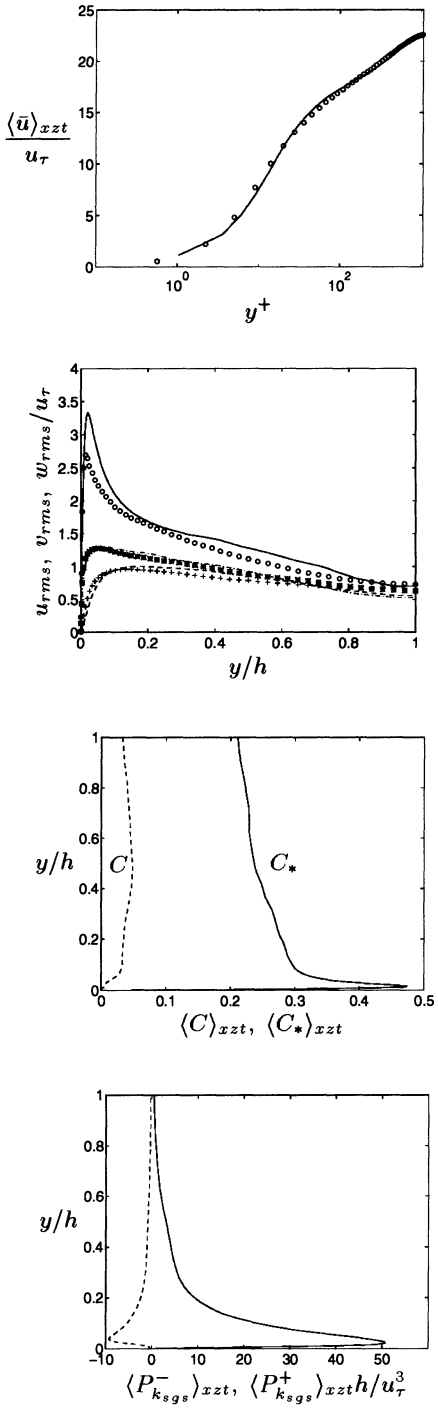

Figure 1: Channel flow. One-equation dynamic model. $Re_\tau = 1050$. Markers: Piomelli (1995).

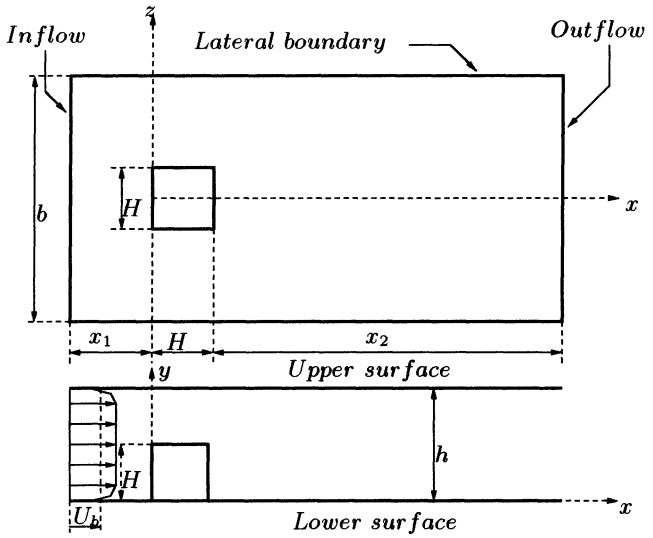

Figure 2: Computational domain for the surface-mounted cube.

Model	$\langle C_L \rangle_t$	$C_{L,rms}$	$\langle C_D \rangle_t$	$C_{D,rms}$
Smagorinsky	0.57	0.033	0.46	0.021
OEM	0.57	0.031	0.47	0.019
No model	0.60	0.025	0.40	0.019

Table 1: Mean and RMS values of lift and drag coefficients.

SURFACE-MOUNTED CUBE

The surface-mounted cubic obstacle is placed on a channel wall at $Re = 40\,000$, based on the incoming mean bulk velocity and the obstacle height. The geometry of the computational domain is given in Fig. 2. For the simulations, a domain with an upstream length of $x_1/H = 3$ and a downstream length of $x_2/H = 6$ was used, while the span-wise width was set at $b/H = 7$. Both the standard Smagorinsky model ($C_s = 0.1$) and the one-equation model (Davidson 1997b), denoted OEM, are used. The series of time-averaged velocities and stresses has been computed (see Fig. 3).

The agreement with the experiments is fairly good. The prediction with models is better than without models, especially in the recirculation region on the roof of the cube. Resolved Reynolds stresses and $\langle u_i^2 \rangle_t + 2\langle k_{sgs} \rangle_t/3$ are plotted along the centreline of the cube in Fig. 4. It can be seen that the SGS stresses are negligible, apart from close to the re-attachment behind the cube. Figure 5a shows streamlines projected onto the surface of the obstacle. The stagnation points on the front and back sides can be seen. Recirculation regions on the lateral sides are also clearly visible. The drag and lift coefficients are presented in Table 1. No experimental values for C_D and C_L are known to the au-

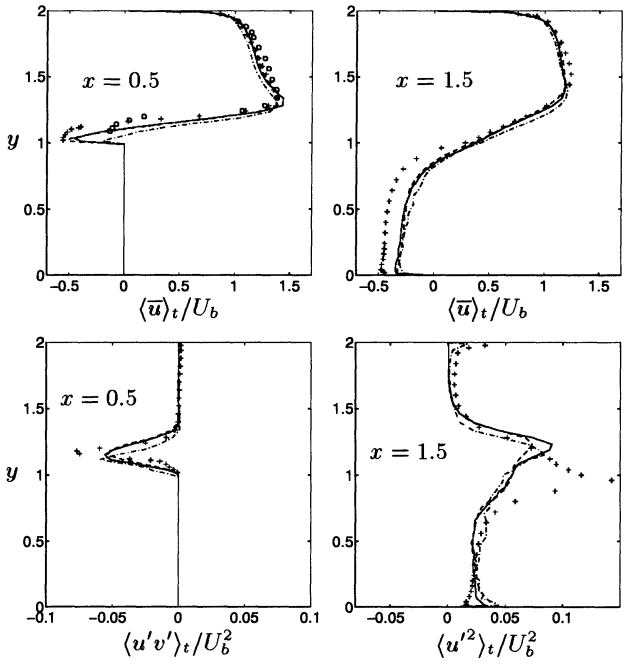

Figure 3: Surface-mounted cube. Comparison between the OEM (dashed line) and Smagorinsky (solid line) and calculation without model (dash-dotted line).

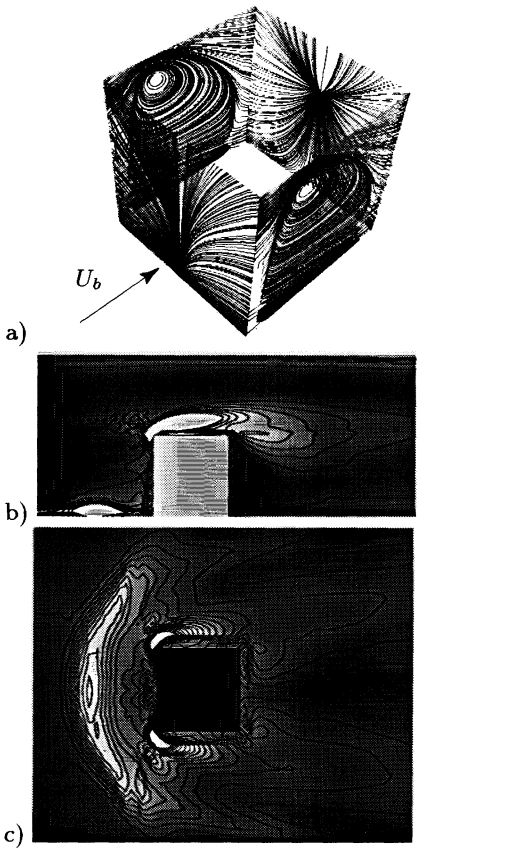

Figure 5: Surface-mounted cube. OEM. a) Streamlines projected onto the surface of the cube. b) Vorticity ω_z, $z = 0$. c) Vorticity ω_y, $y = 0.01$.

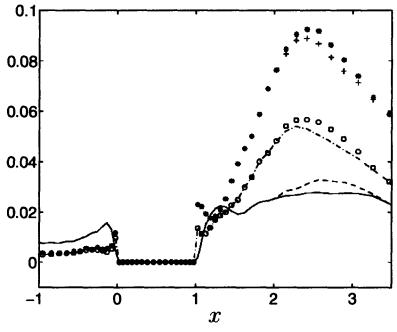

Figure 4: Surface-mounted cube. OEM. a) Normal stresses along the centreline ($y = 0.5, z = 0$) of the cube $\langle u'^2\rangle_t/U_b^2$ (solid line), $(\langle u'^2\rangle_t + 2\langle k_{sgs}\rangle_t/3)/U_b^2$ (dashed lines), $\langle v'^2\rangle_t/U_b^2$ (dash-dotted line), $(\langle v'^2\rangle_t + 2\langle k_{sgs}\rangle_t/3)/U_b^2$ (o), $\langle w'^2\rangle_t/U_b^2$ (+), $(\langle w'^2\rangle_t + 2\langle k_{sgs}\rangle_t/3)/U_b^2$ (*).

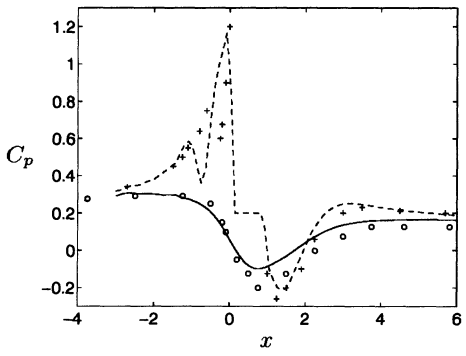

Figure 6: Surface-mounted cube. OEM. Surface pressure coefficient C_p, distribution on the upper channel wall (solid line) and lower channel wall (dashed line). Experiment: upper wall (o); lower wall (+). $z = 0$.

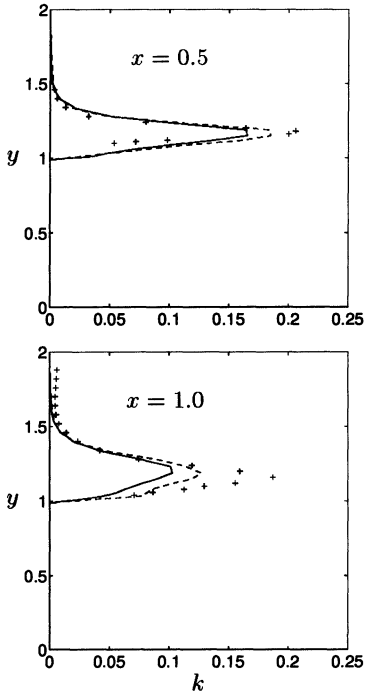

Figure 7: Surface-mounted cube. Comparison between OEM (solid line), Smagorinsky (dashed line). Experiment (markers). Resolved kinetic turbulent energy k.

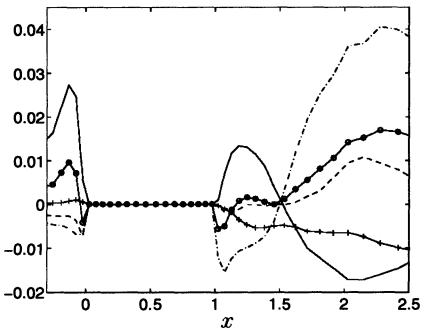

Figure 8: Surface-mounted cube. Resolved production terms along the centreline ($y = 0.5, z = 0$). $\langle P_{uu}\rangle_t$ (solid line), $\langle P_{vv}\rangle_t$ (dashed line), $\langle P_{ww}\rangle_t$ (dash-dotted line), P_{uv} $(-+)$, P_k $(-o)$.

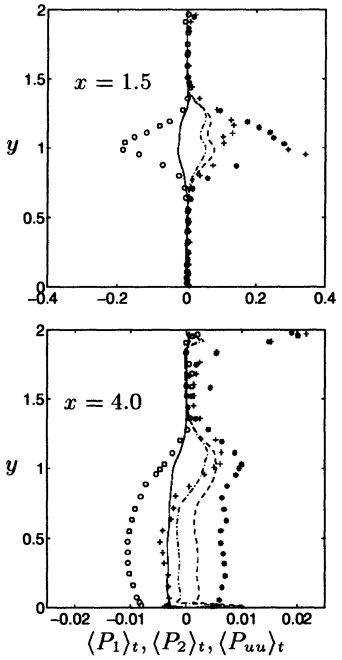

Figure 9: Surface-mounted cube. OEM: $\langle P_1\rangle_t$ (solid line), $\langle P_2\rangle_t$ (dashed line), $\langle P_{uu}\rangle_t$ (dash-dotted line). Experiments: P_1 (o), P_2 $(*)$, P_{uu} $(+)$.

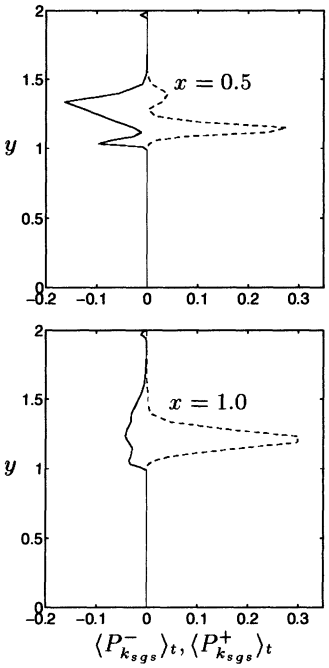

Figure 10: Surface-mounted cube. Production.

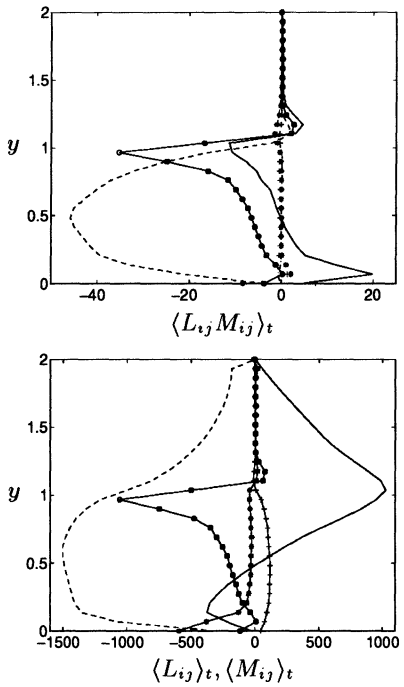

Figure 11: Surface-mounted cube. OEM. $x = -0.2, z = 0.6$. a) Production $\langle P_{k_{sgs}}\rangle_t/300$ is denoted by $-o$. $\langle L_{12}M_{12}\rangle_t$ (solid line), $\langle L_{13}M_{13}\rangle_t$ (dashed line), $\langle L_{22}M_{22}\rangle_t$ (dash-dotted line), $\langle L_{23}M_{23}\rangle_t$ $(**)$, $\langle L_{33}M_{33}\rangle_t$ $(++)$; b) Production $\langle P_{k_{sgs}}\rangle_t/10$ is denoted by $-o$. $\langle L_{12}\rangle_t$ (solid line), $\langle L_{13}\rangle_t$ (dashed line), $\langle M_{12}\rangle_t$ $(-*)$, $\langle M_{13}\rangle_t$ $(-+)$.

thors. The vorticity ω_i is presented in Figs. 5b and 5c. The recirculation zones in front of the cube and on the roof are clearly visible in Fig. 5b. Recirculation zones on the lateral sides and behind the cube can also be seen in Fig. 5c. The horseshoe is visible in Fig. 5c. Figure 6 compares the pressure coefficient C_p for the OEM, along the plane $z/H = 0$. The agreement between predictions is fairly good on the lower wall, whereas the dip in C_p on the upper wall is rather under-predicted, compared to experiment. More results relating to the statistics of the mean flow and global quantities are given in Krajnović (1998) and Krajnović et al. (1999).

RANS quantities

LES results can be used to improve RANS models. We have studied the k equation, where $k = 1/2(u'^2 + v'^2 + w'^2)$. Figure 7 shows a comparison of resolved kinetic energy $\langle k\rangle_t$ and k obtained in experiments (Hussein and Martinuzzi 1996). The local maxima of $\langle k\rangle_t$ correlates with the location of the shear layer as it is observed in the experiments.

The production terms in the k equation were computed in the center plane as:

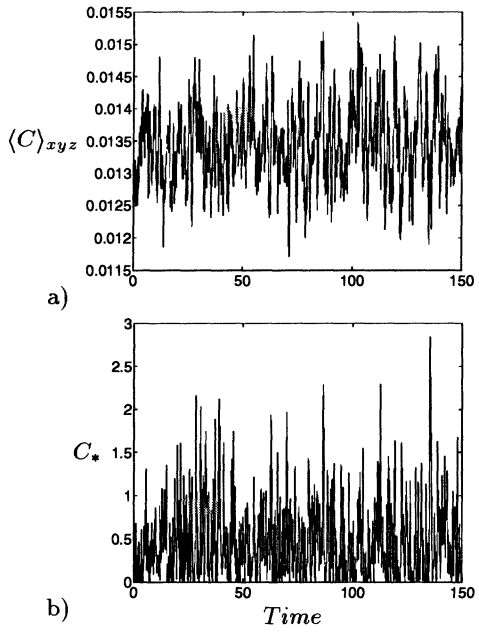

Figure 12: Time history of the dynamic coefficients. a) The dynamic coefficient $\langle C\rangle_{xyz}$; b) The dynamic coefficient C_* at one chosen cell in front of the cube.

$$
\begin{aligned}
P_{uu} &= -2\left(\langle u'^2\rangle_t \frac{\partial\langle\bar{u}\rangle_t}{\partial x} + \langle u'v'\rangle_t \frac{\partial\langle\bar{u}\rangle_t}{\partial y}\right);\\
P_{vv} &= -2\left(\langle v'^2\rangle_t \frac{\partial\langle\bar{v}\rangle_t}{\partial y} + \langle u'v'\rangle_t \frac{\partial\langle\bar{v}\rangle_t}{\partial x}\right);\\
P_{ww} &= -2\langle w'^2\rangle_t \frac{\partial\langle\bar{w}\rangle_t}{\partial z};\\
P_{uv} &= -\langle u'^2\rangle_t \frac{\partial\langle\bar{v}\rangle_t}{\partial x} - \langle v'^2\rangle_t \frac{\partial\langle\bar{u}\rangle_t}{\partial y}\\
&\quad - \langle u'v'\rangle_t \left(\frac{\partial\langle\bar{u}\rangle_t}{\partial x} + \frac{\partial\langle\bar{v}\rangle_t}{\partial y}\right);\ P_k = 0.5P_{ii}.
\end{aligned}
\tag{5}
$$

The resolved production terms are plotted along the centreline in Fig. 8 and normal stresses are shown in Fig. 4.

We start by discussing P_{uu}. $|\langle u'^2\rangle_t \partial\langle\bar{u}\rangle_t/\partial x|$ is much larger than $|\langle u'v'\rangle_t \partial\langle\bar{u}\rangle_t/\partial y|$ in front of the cube. $\partial\langle\bar{u}\rangle_t/\partial x$ is negative and decreases rapidly after the separation in front of the cube and this is why $P_{uu} < 0$. The shear stress $\langle u'v'\rangle_t$ is positive in this region and $\langle u'v'\rangle_t$ is much smaller then $\langle u'^2\rangle_t$. The gradient $\partial\langle\bar{u}\rangle_t/\partial y$ is positive and becomes negative very close to the stagnation point. Behind the cube, $\partial\langle\bar{u}\rangle_t/\partial x$ is negative. It changes sign at $x \approx 1.5$ and, since this term is dominant, P_{uu} also changes sign. $\partial\langle\bar{u}\rangle_t/\partial y$ is positive all the way with a maximum at $x \approx 3$. $\langle u'^2\rangle_t$ has its maximum close to the re-attachment at $x = 2.44$. Also

$\langle u'v' \rangle_t$, which is negative, has its minimum close to the re-attachment. P_{uu} is generally approximately equal to $-2\langle u'^2 \rangle_t \partial \langle \bar{u} \rangle_t / \partial x$.

Next, we consider P_{vv}. In P_{vv}, $\langle v'^2 \rangle_t \partial \langle \bar{v} \rangle_t / \partial y$ is the dominant term. $-\langle v'^2 \rangle_t \partial \langle \bar{v} \rangle_t / \partial y$ is negative in front of the cube. It decreases very rapidly at separation ($x \approx -0.97$). This rapid decrease in $\langle v'^2 \rangle_t \partial \langle \bar{v} \rangle_t / \partial y$ is caused by $\partial \langle \bar{v} \rangle_t / \partial y$, which is positive here and increases at this position. Between the separation and the stagnation point, $\partial \langle \bar{v} \rangle_t / \partial x \approx -\partial \langle \bar{v} \rangle_t / \partial y$. The term $\langle v'^2 \rangle_t \partial \langle \bar{v} \rangle_t / \partial y$ remains negative behind the cube until $x \approx 1.46$. From here on, it increases until it reaches its maximum close to the re-attachment ($x \approx 2.44$). While $\langle v'^2 \rangle_t \partial \langle \bar{v} \rangle_t / \partial y$ approaches its maximum close to the re-attachment point, $\langle u'v' \rangle_t \partial \langle \bar{v} \rangle_t / \partial x$, which is negative, approaches its minimum here. In this region, $\partial \langle \bar{v} \rangle_t / \partial x < 0$, $\partial \langle \bar{v} \rangle_t / \partial y < 0$ and $\langle u'v' \rangle_t < 0$. The stresses $\langle u'v' \rangle_t$ and $\langle v'^2 \rangle_t$ are much larger behind the cube than in front of it.

P_{ww} is negative in front the cube and $P_{ww} \approx P_{vv}$. Behind the cube, P_{ww} is first negative (until $x \approx 1.5$) and then positive. It reaches its maximum at the separation point. The magnitude of P_{uu} is greater than the magnitude of P_{vv} in front of the cube. Here, $|\langle u'^2 \rangle_t \partial \langle \bar{u} \rangle_t / \partial x| \gg |\langle v'^2 \rangle_t \partial \langle \bar{v} \rangle_t / \partial y|$ because $\langle u'^2 \rangle_t > \langle v'^2 \rangle_t$ and $|\partial \langle \bar{u} \rangle_t / \partial x| > |\partial \langle \bar{v} \rangle_t / \partial y|$. Behind the cube, $P_{uu} \gg P_{vv}$, because $|\partial \langle \bar{u} \rangle_t / \partial x| \gg |\partial \langle \bar{v} \rangle_t / \partial y|$. After re-attachment, $P_{uu} \approx -P_{vv}$. In front of the body, P_k increases, as the flow approaches the body. A rapid decrease in P_{vv} near the stagnation point results in a sharp dip in P_k. Similar results are observed in the LES of the flow in tube bundles (Rollet-Miet et al. 1999). The dip in P_k behind the cube is due to a strong decrease in $\langle v'^2 \rangle_t$.

Figure 9 shows $P_1 = -2\langle u'^2 \rangle_t \partial \langle \bar{u} \rangle_t / \partial x$, $P_2 = -2\langle u'v' \rangle_t \partial \langle \bar{u} \rangle_t / \partial y$ and P_{uu} in the recirculation region behind the cube ($x/H = 1.5$) and in the recovery region ($x/H = 4$). The poor agreement with the experiments is due to incorrect LES predictions of the location of the Reynolds stress peak (see Fig. 3).

Backscatter

The production, $P_{k_{sgs}}$, is shown in Fig. 10. We have observed the strongest $\langle P^- \rangle_t$ near the front vertical corners. To explain the reasons for $\langle P^- \rangle_t$, we have computed $\langle L_{ij} M_{ij} \rangle_t$ in the position of the strongest backscatter. It can be seen in Fig. 11a that, in the region of strongest $\langle P^- \rangle_t$, $\langle L_{12} M_{12} \rangle_t$ and $\langle L_{13} M_{13} \rangle_t$ are the dominant terms. L_{13} is the most important negative term, as is shown in Fig. 11b.

The time history of the homogeneous dynamic coefficient $\langle C \rangle_{xyz}$ is shown in Fig. 12a. The time-averaged mean value is close to 0.013. The dynamic coefficient C_* is shown in Fig. 12b. It often tends towards zero but it never becomes larger than 3.

CONCLUSIONS

The one-equation model was used in predictions of channel flow and the flow around a surface-mounted cube. For both flows, good agreement with experiments was found. The phenomenon of "backscatter" was studied and reasons for its prediction are given. The k equation was studied with the aim of improving RANS models.

Acknowledgments

This work was supported by NUTEK (Swedish National Board for Industrial and Technical Development) and the Volvo Car Corporation. The channel computations were supported by the LESFOIL project within the Brite-Euram programme.

References

Davidson, L. (1997a). Large eddy simulation: A dynamic one-equation subgrid model for three-dimensional recirculating flow. In *11th Int. Symp. on Turbulent Shear Flow*, Volume 3, Grenoble, pp. 26.1–26.6.

Davidson, L. (1997b). LES of recirculating flow without any homogeneous direction: A dynamic one-equation subgrid model. In *2nd Int. Symp. on Turbulence Heat and Mass Transfer*, Delft, pp. 481–490. Delft University Press.

Hussein, H. J. and R. J. Martinuzzi (1996). Energy balance for turbulent flow around a surface mounted cube placed in a channel. *Physics of Fluids 8*, 764–780.

Krajnović, S. (1998). Large-eddy simulation of the flow around a surface-mounted single cube in a channel. Rept. 98/7, Dept. of Thermo and Fluid Dynamics, Chalmers University of Technology, Gothenburg.

Krajnović, S., D. Müller, and L. Davidson (1999). Comparison of two one-equation subgrid models in recirculating flows. In *Third ERCOFTAC Workshop on Direct and Large-Eddy Simulation, Cambridge, May 12-14*.

Piomelli, U. (1995). High Reynolds number calculations using the dynamic subgrid-scale stress model. *Physics of Fluids A 5*, 1484–1490.

Piomelli, U., W. Cabot, P. Moin, and S. Lee (1991). Subgrid-scale backscatter in turbulent and transitional flows. *Physics of Fluids A 3*, 1766–1771.

Rollet-Miet, P., D. Laurence, and J. Ferziger (1999). LES and RANS of turbulent flow in tube bundles, to appear in:. *Int. J. Heat and Fluid Flow*.